The Astrophysical Journal, 974:139 (14pp), 2024 October 10 https://doi.org/10.3847/1538-4357/ad6d5b

How Landmass Distribution Influences the Atmospheric Dynamics of Tidally Locked Terrestrial Exoplanets

F. Sainsbury-Martinez[1], C. Walsh[1], G. J. Cooke[1,2], and D. R. Marsh[1]
[1] School of Physics and Astronomy, University of Leeds, Leeds LS2 9JT, UK
[2] Institute of Astronomy, University of Cambridge, UK
Received 2024 July 1; revised 2024 August 5; accepted 2024 August 7; published 2024 October 9

Abstract

Interpretation of the ongoing efforts to simulate the atmospheres of potentially habitable terrestrial exoplanets requires that we understand the underlying dynamics and chemistry of such objects to a much greater degree than 1D or even simple 3D models enable. Here, for the tidally locked habitable-zone planet TRAPPIST-1e, we explore one effect which can shape the dynamics and chemistry of terrestrial planets: the inclusion of an Earth-like land–ocean distribution with orography. To do this we use the Earth-system model WACCM6/CESM2 to run a pair of TRAPPIST-1e models with N_2–O_2 atmospheres and with the substellar point fixed over either land or ocean. The presence of orography shapes atmospheric transport, and in the case of Earth-like orography, breaks the symmetry between the Northern and Southern Hemispheres which was previously found in slab ocean models. For example, peak zonal jet speeds in the Southern Hemisphere are 50%–100% faster than similar jets in the Northern Hemisphere. This also affects the meridional circulation, transporting equatorial material toward the south pole. As a result we also find significant changes in the atmospheric chemistry, including the accumulation of potentially lethal quantities of ozone at both the south pole and the surface. Future studies which investigate the effects of landmass distribution on the dynamics of exoplanetary atmospheres should pay close attention to both the dayside land fraction as well as the orography of the land. Simply modeling a flat landmass will not give a complete picture of its dynamical impact.

Unified Astronomy Thesaurus concepts: Planetary atmospheres (1244); Atmospheric composition (2120); Exoplanet atmospheric dynamics (2307); Computational methods (1965)

Materials only available in the online version of record: animation

1. Introduction

The search for a habitable terrestrial exoplanet remains a tricky prospect, with the transit signal associated with the atmosphere of an Earth-analog planet passing in front of a Sun-like star lying below the current detection limits of both space and ground-based spectrometers. Although future space missions, such as LIFE (Kammerer et al. 2022) or the Habitable Worlds Observatory (National Academies of Sciences & Engineering, and Medicine 2023), may be able to characterize Earth-analog atmospheres. However, planetary systems orbiting cooler stars, particularly M dwarfs, offer a current-day solution to this conundrum. The transits of said planets are generally easier to detect than their G dwarf orbiting counterparts thanks to the significantly smaller radius of M dwarfs increasing the relative signal of both a transiting planet and its extended atmosphere. Furthermore, the lower luminosities of these stars mean that the habitable zone, which is broadly defined as the region around a star in which the equilibrium temperature of a planet would fall into the range that allows for liquid water on the surface, lies much closer to the host star (Kopparapu et al. 2013). For example, the habitable zone of TRAPPIST-1 lies between ∼0.025 and ∼0.05 au (Gillon et al. 2013, 2016), which corresponds to an orbital period of between ∼4.5 and ∼13.5 days. This means that that multiple transits of any potentially habitable planets (such as TRAPPIST-1e, the most likely of the habitable-zone TRAPPIST-1 planets to host a potentially terrestrial atmosphere; Wolf 2017; Krissansen-Totton et al. 2021) can be combined, reducing the signal-to-noise ratio and allowing for the detection of atmospheric constituents within weeks/months rather than years/decades (Lustig-Yaeger et al. 2019).

However, the proximity of such planets to their host star is also likely to have implications for their orbital dynamics. Specifically, the small orbital distance between habitable-zone planets and their host M dwarf star means that angular momentum exchange via tidal torques between the two bodies is likely to lead to the synchronization of the planetary rotation rate and orbital period. This is known as tidal locking and it implies a permanently illuminated dayside and a permanently dark, and hence cooler, nightside (Dole 1964; Barnes 2017). This is likely to have significant implications for the atmospheric dynamics, with the strong day–night temperature–pressure gradient acting as one of the primary drivers of the global circulation. The other driver of the atmospheric dynamics is, of course, the somewhat rapid planetary rotation ($P_{\rm rot} < 15$ days), with the Coriolis effect playing a significant role in shaping any off-equator circulations. On the Earth these effects include the geostrophic winds that drive the extra-tropical cyclones/anticyclones that are responsible for much of the US's and Europe's weather (Hoskins & Valdes 1990; Chang et al. 2002; Laurila et al. 2021).

Taken together, the fixed stellar insolation and the strong off-equator Coriolis effect can lead to the formation of standing Rossby and Kelvin waves, which pump eastwards angular momentum from high latitudes toward the equator, a process

that can result in the formation of (a) superrotating jet(s) (Showman & Polvani 2011). Such a process has been predicted (Showman & Guillot 2002) and observed (Knutson et al. 2007; Zellem et al. 2014) for hot Jupiters (Jupiter-sized planets which orbit close to their host star) and is also expected to play an import role in the atmospheric dynamics, and chemistry, of terrestrial exoplanets (e.g., Carone et al. 2014, 2015, 2015).

Recently, Braam et al. (2023) used an Earth-like global circulation model (GCM) of Proxima Centauri b to suggest that a stratospheric dayside-to-nightside overturning circulation should advect ozone from its formation location on the dayside to the nightside. Here ozone persists due to a combination of a lack of UV irradiation to drive photolytic loss processes and confinement in off-equator gyres associated with global standing Rossby and Kelvin waves. However the hemispherically symmetric winds found by Braam et al. (2023) are likely only possible thanks to their use of a global slab ocean (i.e., a motionless ocean, which is assumed to be well mixed and covers the entire planetary surface) instead of a dynamic ocean or accounting for the presence of landmasses. The inclusion of a dynamic ocean can significantly alter heat transport, including day–night heat transport, thus affecting the day–night temperature contrast and hence the strength of the global overturning circulation (Hu & Yang 2014). The inclusion of landmasses can break global wind symmetries (as on Earth) and affect the circulations found in a dynamic ocean (Salazar et al. 2020). A good example of the effect that landmasses can have on the global symmetries of atmospheric circulations is Del Genio et al. (2019), who explored models of Proxima Centauri b with Earth-like landmass distributions and found that the topography reshaped winds, breaking symmetries including the location of (Rossby) gyres. However they did not include a coupled chemistry scheme in their model, and hence were unable to investigate, for example, the effects of landmasses on the ozone distribution. Since then, such a model has been run: Bhongade et al. (2024) showed that, when including an Earth-like land–ocean distribution in a model of the tidally locked terrestrial exoplanet TRAPPIST-1e, any symmetry in the ozone distribution goes away. Instead the ozone accumulates over the south pole due to a combination of the same overturning circulations as in Braam et al. (2023), transporting ozone from the dayside to the nightside in the outer atmosphere, and an asymmetry in the near-surface winds on the nightside transporting material southward. They attribute the asymmetry in the near-surface winds to wave breaking associated with the land–ocean boundaries (for more details of these effects see, for example, Broccoli & Manabe 1992; Sandu et al. 2019; Pepin et al. 2022, 2022). Note that a similar result was found by Cooke et al. (2024), who discuss how the cold nightside allows for the accumulation of potentially lethal (>40 ppbv) levels of surface ozone on tidally locked exoplanets.

In this work we explore how the presence of Earth-like orography affects the atmospheric dynamics of terrestrial exoplanets in more detail, including investigating if the global atmospheric circulations (and resulting advection of ozone) are affected by the land–ocean distribution at the substellar point.

In Section 2 we introduce our model, WACCM6/version 2 of the Coupled Earth System Model (CESM2), an Earth system model which has been used to study the atmospheres of both Earth-analog (Cooke et al. 2022; Liu et al. 2023) and tidally locked (Cooke et al. 2023; Bhongade et al. 2024; Cooke et al. 2024) exoplanets with preindustrial Earth-like atmospheric compositions and landmass distributions. Here we use WACCM6/CESM2 to run two models of TRAPPIST-1e, one in which the substellar point is fixed over the Pacific Ocean and one in which it is fixed over land (specifically central Africa). Note that this pair of relative landmass distributions is the same as was considered by Del Genio et al. (2019), allowing us to, much like them, explore if the presence of a landmass at the substellar point has a significant effect on the atmospheric dynamics and, using our coupled model, chemistry. In Section 3 we compare and contrast the aforementioned models in more detail. This includes exploring differences in global atmospheric chemistry, differences (and similarities) in both zonal and meridional flows, and how orography shapes the horizontal winds by acting as a local source of divergence and vorticity. We also investigate how the winds shape the ozone distribution, driving the accumulation over the south pole (Antarctic) found by both Bhongade et al. (2024) and Cooke et al. (2024). We finish, in Section 4, with some concluding remarks, discussing the implications of our results as well as the need for future model development of more flexible landmass and orography models which can be coupled with models like WACCM6/CESM2 in order to better understand how such effects, and the associated symmetry breaking, might shape future observations of the atmospheres of potentially habitable exoplanets.

2. Method: Modeling TRAPPIST-1e with WACCM6/CESM2

To understand how the land–ocean distribution can shape the winds and resulting atmospheric chemistry of tidally locked terrestrial exoplanets, we explore the atmospheric dynamics found in two tidally locked TRAPPIST-1e models based upon the work of Cooke et al. (2023). These models are based on a version of WACCM6/CESM2 which has been modified to account for synchronous rotation[3] (i.e., a tidally locked planet in which the location of the incoming stellar insolation is fixed).

WACCM6 is a well-documented (Gettelman et al. 2019) high-top (the atmosphere extends to ∼140 km above the surface) configuration of CESM2. It includes a modern, Earth-like, ocean and land model (including orography), and an initial atmospheric composition which approximates the preindustrial Earth. That is to say an Earth-like atmosphere, primarily composed of nitrogen and oxygen, with smaller amounts of water vapor, methane, carbon dioxide, and lighter noble gases. It does not include any human-induced changes, such as pollution or greenhouse gas enhancement. For instance, the atmosphere is 285 ppm CO_2 versus the present-day value of >420 ppm. Horizontally, both simulations have a resolution of $1^{\circ}.875$ by $2^{\circ}.5$ (corresponding to 96 cells latitudinally and 144 cells longitudinally), while vertically the simulation domain is split into 70 atmospheric levels distributed between 1 and 4.5×10^{-9} bar, in $\log(P)$ space, such that the number of pressure levels increases near the surface (where the atmosphere is more dynamically active). Finally both models have been integrated for over 300 yr (with a 30 minute time step) in order to ensure that any effects associated with the atmospheric dynamics settling into a state associated with synchronous rotation have dissipated. For example, we find no long-term trends in the atmospheric or surface temperature. For our

[3] github.com/exo-cesm/

Table 1
Planetary Parameters of TRAPPIST-1e, Taken from Delrez et al. (2018), Grimm et al. (2018), and Agol et al. (2021), with the Final Mass and Radius of the Planet Being Chosen Such as to Be Consistent with the TRAPPIST-1 Habitable Atmosphere Intercomparison Program (Fauchez et al. 2022; Sergeev et al. 2022; Turbet et al. 2022)

Parameter	Value	Unit
Radius R	0.91	$R_\oplus$
Mass M	0.772	$M_\oplus$
Semimajor Axis a	0.0292	au
Orbital Period $P_{\rm orb}$	6.099	days
Obliquity ϵ	0	
Eccentricity e	0	
Peak Insolation I	900	W m^{-2}
Surface Gravity g	9.1454	m s^{-2}

analysis, we consider a temporal average over the last 30 yr of simulation time. A more in-depth discussion of WACCM6/CESM2, including the chemistry, radiation, and cloud physics, can be found in Cooke et al. (2023) and Liu et al. (2023). More details on the Earth-tuned chemical network can be found in Gettelman et al. (2019) and Emmons et al. (2020).

TRAPPIST-1e is a terrestrial planet which remains a strong object of interest in the ongoing search for a habitable, terrestrial, exoplanet. It has a radius of 0.91 $R_\oplus$ and an orbital period of only ∼6.1 days. However, because TRAPPIST-1 is a cool M dwarf, the peak insolation is close to that received by the Earth at 900 W m^{-2} (around 66% of that received by the Earth, but 50% more than Mars), placing the planet at the cooler edge of the habitable zone (see Table 1 for more details). To match this peak insolation, we rescale the TRAPPIST-1 spectrum of Peacock et al. (2019; calculated using the PHOENIX stellar atmospheric code; Hauschildt 1993; Hauschildt & Baron 2006; Baron & Hauschildt 2007) following the methodology of Cooke et al. (2023). That is to say we rescale the integrated flux to match that received by TRAPPIST-1e while also rebinning the spectrum onto the grid used by WACCM6/CESM2.

The resulting insolation maps can be seen in Figure 1, which also reveals the main difference between the two models considered here: one has the substellar point fixed over the pacific ocean (henceforth referred to as SSPO), while the other has the substellar point fixed over central Africa (henceforth referred to as SSPL). We select these two scenarios to examine which has a greater controlling effect on the global atmospheric dynamics of a tidally locked planet: the presence of land/ocean at the substellar point, or differences in the landmass distribution (and associated orography) between the Northern and Southern Hemispheres. The latter scenario is of particular interest for an Earth-like landmass distribution in which 68% of the land can be found in the Northern Hemisphere, opening up the possibility of significant symmetry breaking between near-surface flows in the Northern and Southern Hemispheres. As previously discussed, and explored here, such asymmetries may play a key role in understanding differences between the latitudinally symmetric and asymmetric ozone distributions of Braam et al. (2023), Bhongade et al. (2024), and Cooke et al. (2024).

2.1. The Helmholtz-wind Decomposition

In order to investigate the horizontal wind dynamics in more detail, including how the surface drives wind asymmetries and

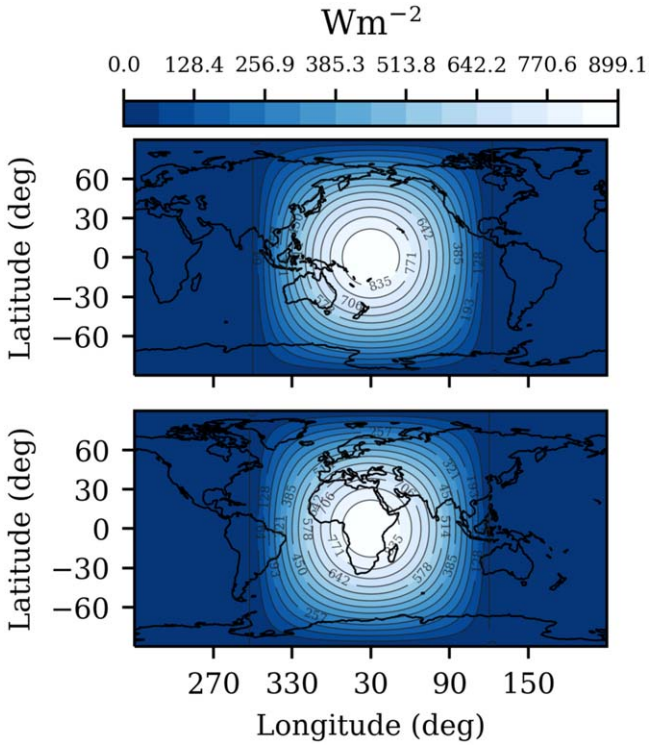

Figure 1. Maps showing the stellar insolation profiles for the two models considered here: one with the substellar point placed over the pacific ocean (SSPO; top), and one with the substellar point placed over land, specifically central Africa (SSPL; bottom). In both maps the landmass distribution is outlined in black.

fixed day–night forcing drives day-to-night transport, we turn to the Helmholtz-wind decomposition, which has long been a staple of Earth atmospheric studies (Dutton 1986) and which has been applied to both hot Jupiters (Hammond & Lewis 2021) and tidally locked terrestrial exoplanets (Sergeev et al. 2022).

The Helmholtz-wind decomposition splits the horizontal wind, $\boldsymbol{u} = (u, v)$ into two components: a divergent component which is "vorticity free" ($\boldsymbol{u}_d$) and a rotational component which is "divergence free" ($\boldsymbol{u}_r$), i.e.:

$$\boldsymbol{u} = \boldsymbol{u}_d + \boldsymbol{u}_r, \tag{1}$$

$$= -\boldsymbol{\nabla}\chi + \boldsymbol{k} \times \boldsymbol{\nabla}\psi, \tag{2}$$

where $\boldsymbol{k}$ denotes a unit vector in the eastward, zonal direction, χ is the velocity potential function, ψ is the velocity streamfunction, and both χ and ψ can be linked to the divergence δ or vorticity w directly:

$$\nabla^2\chi = \delta, \tag{3}$$

$$\nabla^2\psi = w. \tag{4}$$

The rotational component of the wind can be further split into eddy ($\boldsymbol{u}_e$) and zonal-mean ($\boldsymbol{u}_z$) components in order to isolate any zonal jets from rotational wind dynamics that they might be masking:

$$\boldsymbol{u}_z = \langle \boldsymbol{u}_r \rangle, \tag{5}$$

$$\boldsymbol{u}_e = \boldsymbol{u}_r - \boldsymbol{u}_z, \tag{6}$$

where $\langle\rangle$ indicates a zonal mean.

Hence each component of the Helmholtz-wind decomposition probes a different part of the wind. For example, for a tidally locked planet, $\boldsymbol{u}_d$ probes the global overturning

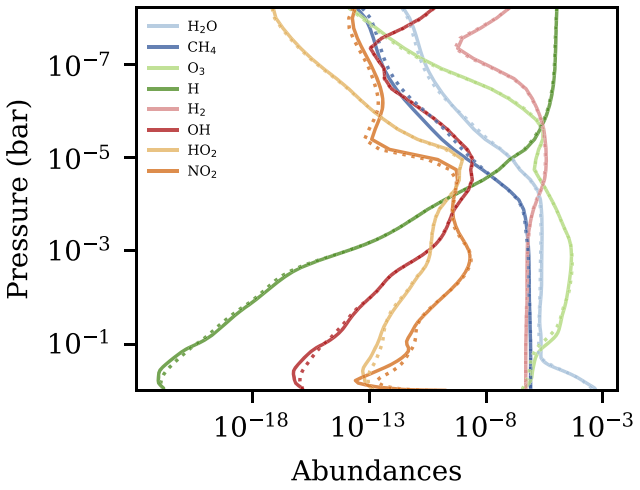

Figure 2. Comparison of the global and temporal mean fractional abundance profiles of eight potentially observable (i.e., H_2O, CH_4, and O_3) or chemically important (i.e., H, H_2, OH, HO_2, and NO_2) atoms and molecules. Profiles extracted from the model with the substellar point placed over the ocean (SSPO) are shown as solid lines, while profiles extracted from the model with the substellar point placed over land/Africa (SSPL) are shown as dashed lines.

circulation while $\boldsymbol{u}_r$ probes the dynamics driven by angular momentum transport including zonal jets ($\boldsymbol{u}_z$) and the standing Rossby and Kelvin waves which drive them ($\boldsymbol{u}_e$).

3. Results

In order to investigate how differences in the landmass distribution at the substellar point, and between the Northern and Southern Hemispheres, affects the atmospheric chemistry and dynamics of tidally locked terrestrial (Earth-analog) exoplanets, we start by examining the global atmospheric chemistry (Section 3.1). We then focus most of our analysis efforts on the atmospheric circulations starting with the zonal-mean dynamics (Section 3.2) before moving onto horizontal wind (Section 3.3) and how the dynamics are shaped by orography (Section 3.4). We finish with a discussion of the ozone distribution, focusing on the accumulation of ozone over the south pole due to orographically induced vortices (Section 3.5).

3.1. Global Atmospheric Chemistry

Figure 2 shows the global and temporal mean fractional abundance profiles of eight atoms/molecules, which are either potentially observable (i.e., H_2O, CH_4, and O_3) or play a significant role in shaping the atmospheric chemistry (i.e., H, H_2, OH, HO_2, and NO_2).

Generally, the differences between the SSPO and SSPL models are small, and hence likely difficult to distinguish observationally. They can also be linked to a single primary driver: the relative influence of a liquid ocean at the substellar point. As discussed in Macdonald et al. (2022, 2024), due to evaporation the fraction of the area around the substellar point which is covered by oceans or land can have a significant effect on the water vapor content of the atmosphere. This is especially true for planets like TRAPPIST-1e (or as they consider, Proxima Centauri b), which not only receive less insolation from their host stars than the Earth does from the Sun, and hence are expected to be cooler, but are also tidally locked, which results in a cold, unirradiated nightside. Together these factors can lead to a large fraction of their ocean away from the "hot" dayside being frozen (Pierrehumbert 2011; Del Genio et al. 2019; Turbet et al. 2022; Cooke et al. 2023). Indeed in both of our models we find that, away from the substellar point, the ocean is entirely frozen over (not shown), leaving our SSPO model in the so-called "Eyeball Earth" state with a liquid ocean at the substellar point, and our SSPL model, with only narrow regions of liquid water near the coastline of Africa.

This difference in liquid-ocean coverage leads to differences in the rate of evaporation of water from the surface, affecting/enhancing the overall water content of the atmosphere. Since this water evaporates on the dayside, it can then undergo photolysis, leading to an enhancement in both the oxygen and hydrogen content of the atmosphere. This oxygen can then go on to form other molecules, including (but not limited to) ozone, which may explain the enhanced ozone content that is hinted at in Figure 2 (see the difference in ozone concentration both at low pressures, where it forms, and near the surface, around 0.1 bar), and seen in both the SSPO/SSPL models of Cooke et al. (2024) and ourselves (Section 3.5).

Overall it is the presence of this liquid ocean which drives many of the differences in atmospheric chemistry seen in Figure 2: the near-surface differences are generally caused by the evaporation of water from the liquid ocean in the SSPO case (thus increasing the overall amount of hydrogen and oxygen in the atmosphere), while the high-altitude changes, in particular the enrichment of oxygen-rich molecules, is due to water undergoing significant UV irradiation and photodissociating. But how does this water get here, and why do we find an enrichment in ozone near the surface for our SSPO model?

3.2. Zonal and Meridional Flows

To understand this transport, as well as the connection between the hot dayside and cold nightside, we next turn to the zonal-wind (Figure 3) and meridional circulation (Figure 4).

Figure 3 shows the zonal-mean zonal wind ($\langle u \rangle$) for both our SSPO (left) and SSPL (right) cases. Here we can clearly see the similarities between the zonal winds in both models. We find three pairs of eastward zonal jets. In the outer atmosphere we find a pair of relatively symmetric jets, centered at $\sim 10^{-5}$ bar ($\sim$70 km altitude) and $\sim \pm 50°$ latitude. Moving deeper, into the middle atmosphere, at a pressure of $\sim 3 \times 10^{-3}$ bar ($\sim$37 km altitude) we find a pair of jets with a strong asymmetry in location between the Southern ($-25°$) and Northern ($\sim 50°$) Hemispheres. Finally, nearer the surface, at a pressure of $\sim$0.5 bar ($\sim$8 km altitude) and a latitude of $\sim \pm 50°$ we find a pair of jets with a strong asymmetry in peak jet speed, with the Southern Hemisphere jet being almost twice as fast (54–60 m s^{-1}) as the jet found in the Northern Hemisphere (31–34 m s^{-1}). The strong similarities between the zonal winds found in the SSPO and SSPL models, coupled with both models exhibiting a significant asymmetry between the Northern and Southern Hemispheres, suggests that the primary driver of circulation asymmetries in our models is not the presence, or lack thereof, of a landmass as the substellar point, but rather differences between the dynamics in the Northern and Southern Hemispheres. As we will discuss in Sections 3.3 and 3.4, the difference between the two hemispheres that is most likely to be responsible is the landmass distribution (with 68% of the land lying in the Northern Hemisphere) and the associated orography.

Next, as shown in Figure 4, we look at the meridional mass streamfunction (meridional circulation), investigating

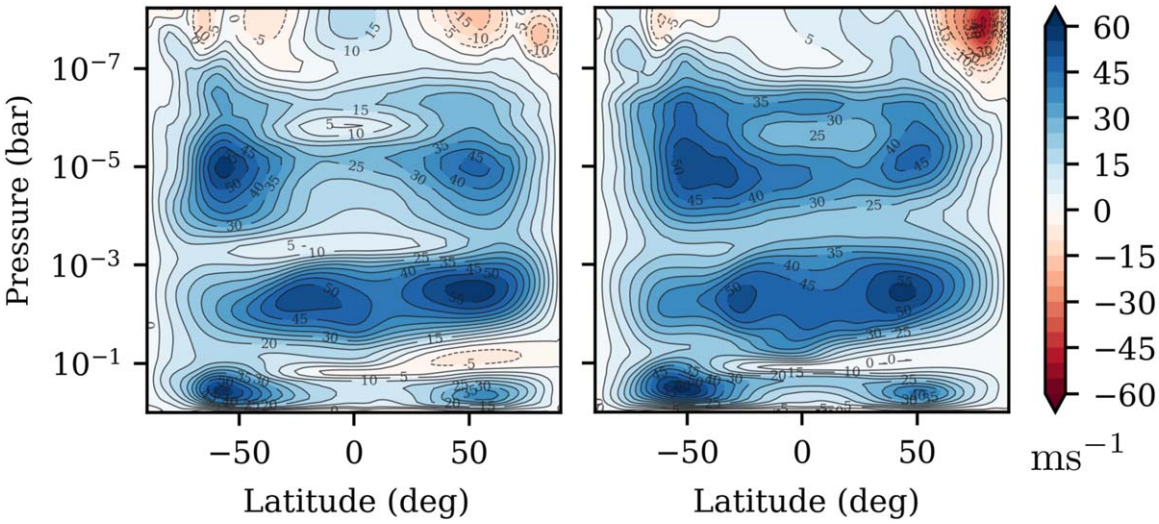

Figure 3. Zonally and temporally averaged zonal-wind profiles for both our model with the substellar point placed over the ocean (SSPO; left) and substellar point placed over land/Africa (SSPL; right). Here eastwards winds are shown in shades of blue while westwards winds are shown in shades of red.

differences not only between our SSPO and SSPL models but also between the zonal-mean circulation and the localized circulation at the substellar and antistellar points.

The meridional mass streamfunction takes the form:

$$\psi = \frac{2\pi R_p}{g \cos\theta} \int_{P_{\rm top}}^{P_0} v \, dP, \tag{7}$$

where v is the meridional velocity, R_p is the radius of the planet, g is the surface gravity, θ is the latitude, and P_0 and $P_{\rm top}$ are the pressure at the surface and top of the atmosphere, respectively. It describes the transport of material in the meridional plane (essentially a slice of the atmosphere taken at a single longitude, or averaged zonally when appropriate), and the interpretation of the figure is rather different from a wind map. Rather than the streamfunction representing flows directly it instead represents circulations. For example, in Figure 4, clockwise circulations are shown in red, while anticlockwise circulations are shown in blue. Where these circulations meet then represents net flows, either latitudinally or vertically. An example of this can be seen for pressures $> 10^{-3}$ bar in the zonal-mean circulations (Figures 4(A) and (B)). Here, the clockwise cell in the Northern Hemisphere and the anticlockwise cell in the Southern Hemisphere combine to drive an upflow slightly north of the equator.

In general, we find that the aforementioned zonal-mean meridional circulation profiles are remarkably similar between our SSPO and SSPL models, with the main difference being the addition, in our SSPO model, of small clockwise circulations at the equator (at $P = 10^{-1}$ bar) and south pole (at $P \simeq 0.5$ bar), circulations which are not enough to overly affect the overall sense of the meridional transport, particularly at higher pressures. For pressures $> 10^{-3}$ bar we find that material is transported downwards at the poles, equatorward at the surface, and generally upwards at the equator, although the symmetry is slightly broken and the upward transport tends to occur slightly off equator in the Northern Hemisphere. Both aspects of this circulation are somewhat reminiscent of the Earth: the circulation cells resemble Hadley cells (see, for example, the review of Xian et al. 2021), albeit rather than extending from the equator to the tropics they extend all the way from the equator to the poles. The northward shift of the upflow away from the equator is similar to the offset seen in the intertropical convergence zone (i.e., Hadley-cell convergence zone; for more details see, for example, Waliser & Jiang 2015; Cheng et al. 2022). A similar single-cell-per-hemisphere structure was found by Braam et al. (2023), although their circulation was symmetric about the equator, which further reinforces our conclusion that the inclusion of an Earth-like landmass distribution has significantly altered the dynamics between the Northern and Southern Hemispheres. Such a conclusion would also explain why, as we move to lower pressures, the differences between our circulation and that of Braam et al. (2023) reduce, with both sets of models revealing a series of alternating clockwise and anticlockwise circulations, likely associated with the strong thermal forcing of the outer atmosphere. Finally, it has been found that rotation can play a role in shaping the extent of the Hadley cell. For example, del Genio & Suozzo (1987) found that, as you slow the rotation of an Earth-like planet, the latitudinal extent of the Hadley cell grows, approaching the poles for rotation periods > 10 days. Similar results are also reported by, for example, Williams (1988a, 1988b), Navarra & Boccaletti (2002), Carone et al. (2014, 2015), Haqq-Misra et al. (2018), Guendelman & Kaspi (2018), among others. Note however that, that the circulations found are generally symmetric about the equator, driven by a lack of symmetry breaking landmasses.

Moving onto the circulation at the substellar point (Figures 4(C) and (D)), we find that, while differences between the SSPO and SSPL models have grown very slightly, the profiles still remain highly similar. Near the surface we find that the circulation consists of two cells in each hemisphere: Hadley-like cells at low latitudes, which drive a net upflow at the equator, braced by Ferrel-like cells that extend from midlatitudes to the poles. In the SSPO model the cells are somewhat symmetric between the Northern and Southern Hemispheres, an effect which can be linked to the fact that we find ocean at almost all substellar latitudes in this model. On the other hand, the role that the landmasses play in shaping the wind are much more apparent in the SSPL model, with the Hadley–Ferrel cell transition occurring around the same latitude that land gives way to ocean in both the Southern

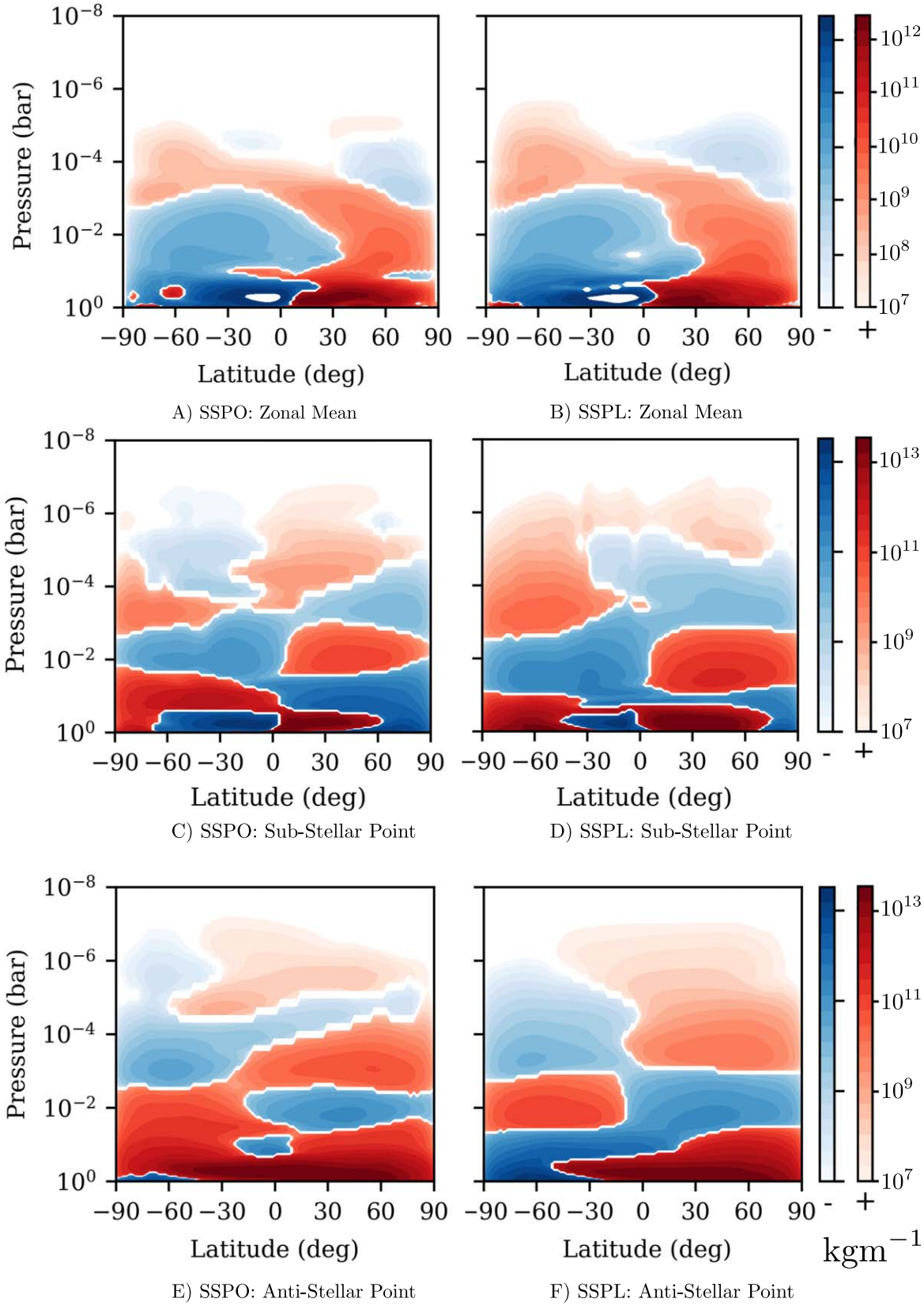

Figure 4. Select temporally averaged meridional circulation streamfunctions for both our model with the substellar point placed over the ocean (SSPO; left) and substellar point placed over land/Africa (SSPL; right). To demonstrate how the combination of tidally locked thermal forcing and Earth-like orography shapes the atmospheric circulations, we show three different views of this circulation: the zonal-mean circulation (top), a 5° average over substellar longitudes (middle), and a 5° average over antistellar longitudes (bottom). Note that the meridional circulation profile is plotted on a log scale with clockwise circulations shown in red and anticlockwise circulations shown in blue. Thus, for example, in the zonal-mean circulation profiles, we find that the clockwise cell in the Northern Hemisphere and the anticlockwise cell in the Southern Hemisphere combine to drive a near equatorial upflow at all pressures greater than 10^{-3} bar.

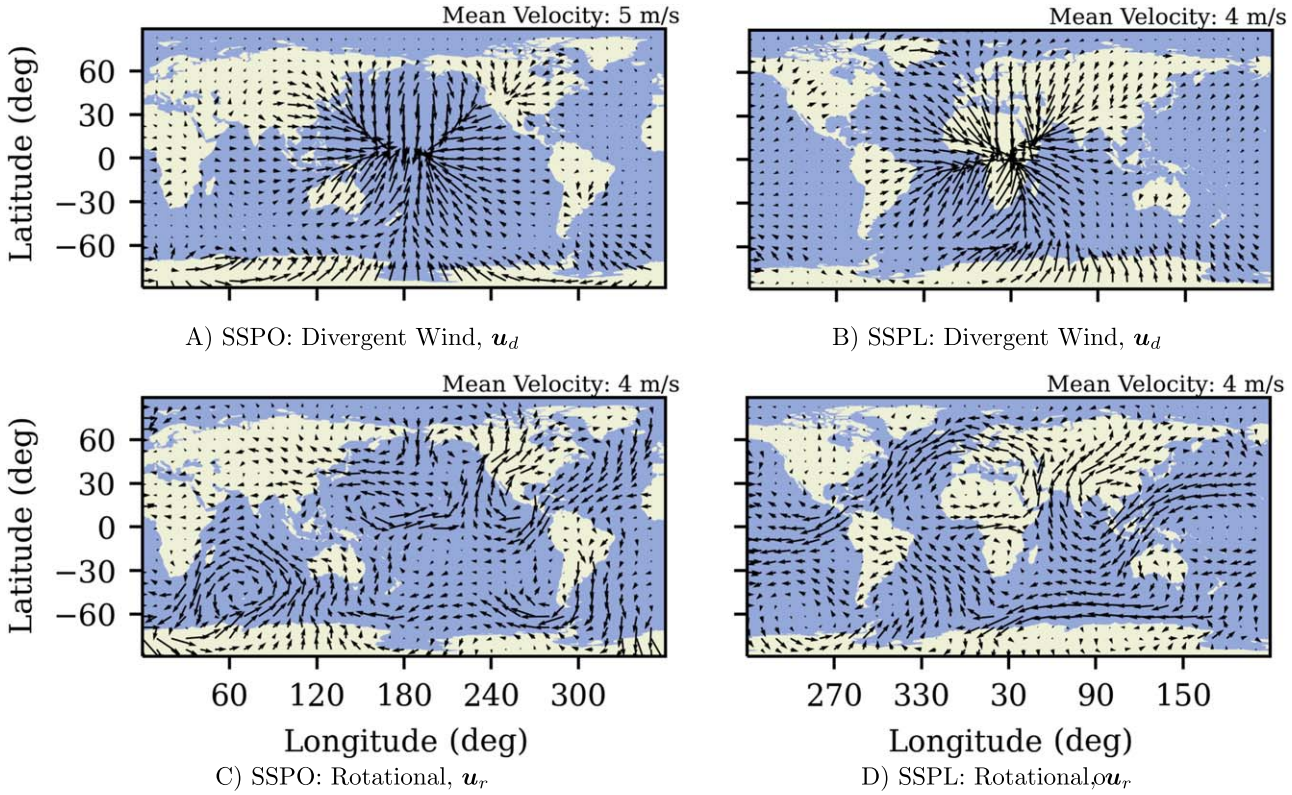

Figure 5. Helmholtz decomposition of the radially averaged near-surface (over all $P > 10^{-1}$ bar) horizontal winds for both our model with the substellar point placed over the ocean (SSPO; right) and the substellar point placed over land/Africa (SSPL; right). The top row plots the divergent component of the wind (U_d) while the bottom row plots the rotational component of the wind (U_r). Landmasses and oceans are shown in green and blue, respectively.

(∼30°–∼40°) and Northern (∼70°) Hemispheres (see Figure 1). Moving to lower pressure we find a stack of alternating clockwise and anticlockwise cells, albeit with differences in the vertical extent of the cells between 10^{-3} and 10^{-1} bar, again likely due to differences in the wind induced by the land distribution and orography. Finally, at low pressures ($P \lesssim 10^{-3}$ bar) the circulation becomes highly time and longitude dependent, much more so than the low-pressure circulations on the nightside (see below), which suggests that the strong thermal forcing drives a highly dynamic atmosphere.

A parallel story of similar circulations in the SSPO and SSPL models holds true near the antistellar point (Figures 4(E) and (F)). Here we find a highly asymmetric circulation structure near the surface, with a single clockwise circulation cell extending from the north pole to a latitude of ∼−50° in the SSPL model and all the way to the south pole in the SSPO model (although the circulation also departs from the surface at a latitude of ∼−50°). Overall, via a series of stacked circulation cells which extend to $\sim 10^{-5}$ bar, we find that material will be transported from the outer atmosphere down toward the surface, where it will then be transported south toward the Antarctic. Furthermore, the differences between the near-surface transport found in the Southern Hemisphere of the SSPO and SSPL models may also explain the difference in peak ozone concentration found by Cooke et al. (2024). In the SSPL model, the southward surface transport does not extend all the way to the south pole, hence we must rely on a smaller anticlockwise circulation cell to complete the poleward transport. This circulation may transport material aloft, reducing the overall concentration of ozone at the pole/surface.

3.3. Helmholtz-wind Decomposition

In order to investigate the effects of the landmass distribution and orography on the atmospheric dynamics, we turn to the Helmholtz-wind decomposition (Section 2.1), which isolates different components of the wind, each of which is has a different underlying driving mechanism.

We start by analyzing the divergent (top row) and rotational (bottom row) components of the near-surface horizontal wind (averaged over $P > 10^{-1}$ bar), as shown in Figure 5, in order to explore how the landmass distribution and orography shape the dynamics.

Near the surface, the divergent component of the wind in both the SSPO and SSPL models (Figures 5(A) and (B)) is dominated by a strong convergence at the substellar point. This is the bottom of the dayside component of the global overturning circulation, which consists of heat rising on the dayside and sinking on the nightside. Note that the top, divergent part of this upwelling can be seen in the radial mean divergent wind, as shown in Figure 6. However, while this convergent wind dominates the profile, the effects of land/orography on the wind can also be felt. For example, consider the divergent winds over the mountainous regions of western North and South America, i.e., the American Cordillera. In North America we find that winds either break up (SSPO) or form (SSPL) over the mountainous region, while in South America we find a consistent divergence from the narrow mountainous band in both models. Similar effects can be seen in the High-Mountain region of Asia centered over the Tibetan Plateau as well as in mountainous regions of Europe and Oceania, although the later is sensitive to the wind convergence at the substellar point. We also find that Antarctica plays a

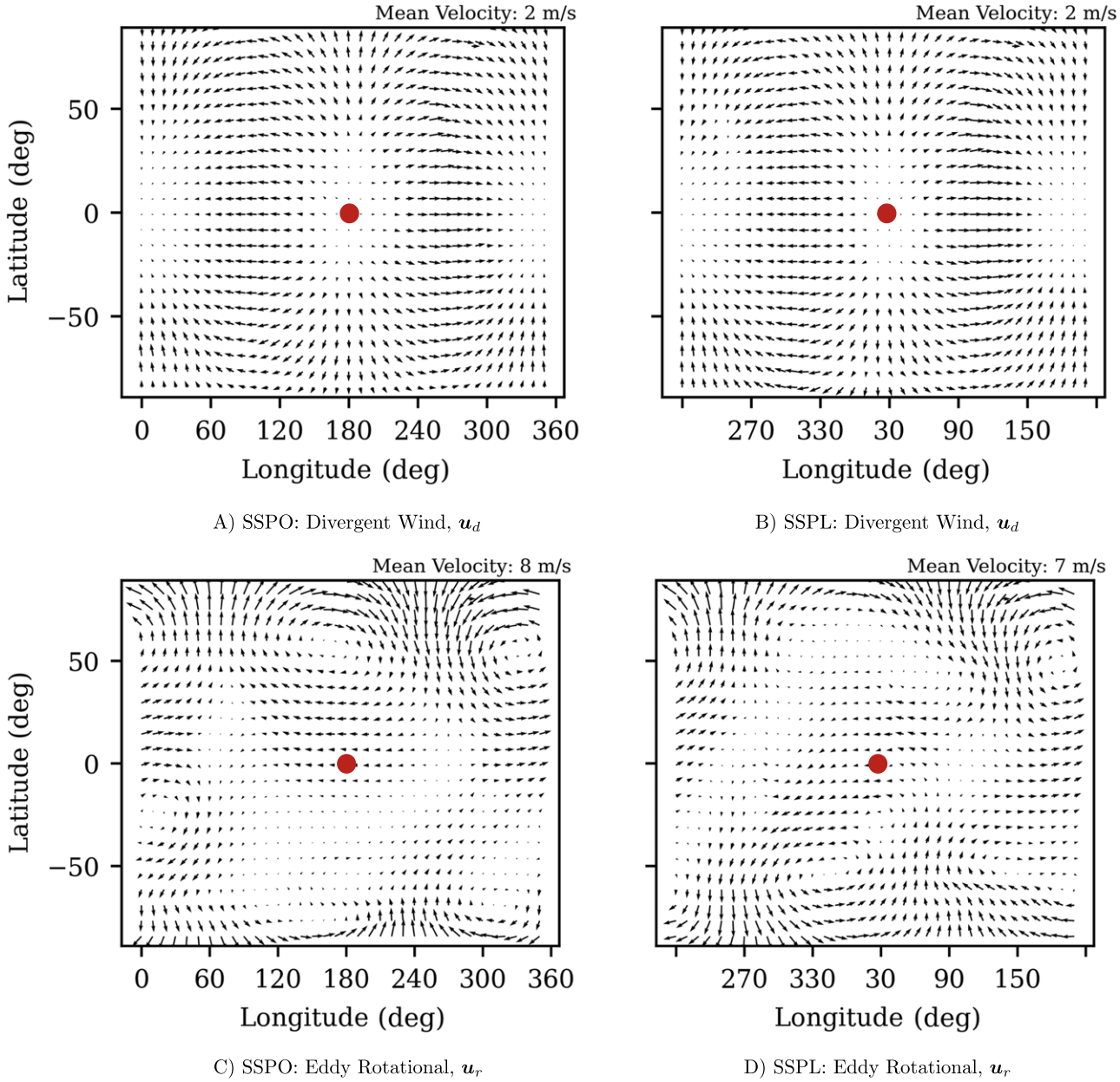

Figure 6. Helmholtz decomposition of the vertically averaged horizontal winds for both our SSPO (left) and SSPL (right) models. The top row plots the divergent component of the wind (U_d) while the bottom row plots the eddy component of the rotational wind (U_e, chosen to emphasizes the standing-wave structure which drives the zonal jets). The location of the substellar point is marked with a red spot. An animated version of this figure showing how the divergent and eddy winds vary with pressure is available online.

(An animation of this figure is available in the online article.)

significant role in shaping the winds in the Southern Hemisphere, driving significant divergent flows northwards. Again this can be linked to the orography of the region: Antarctica is a highly mountainous and high-altitude region (with an average elevation of ∼2500 m), which drives strong katabatic winds from the interior down the steep vertical drops along the coast. Briefly, katabatic winds are gravity-driven flows of cold, dense air parcels from high altitudes to low. They occur because of radiative cooling of air parcels at high altitudes, which itself is driven by the relative coolness of high-altitude landmasses. On Earth, the strongest katabatic winds are associated with the ice sheets of Antarctica and Greenland.

The effects of the landmasses/orography can also be seen in the rotational component of the near-surface wind (Figures 5(C) and (D)), which shows significant differences not only between the Northern and Southern Hemispheres but also between flows over land and oceans. A good example of how the landmass distribution shapes the rotational winds can be seen in Central America (SSPO) and southeast Asia (SSPL). These winds occur at a similar location with respect to the substellar point in both the SSPO and SSPL cases, and in both cases we can see how the flow narrows and intensifies as it passes between two significant landmasses. Furthermore, if we compare the winds over either Asia or South America, we can see how the presence of orography/mountain ranges both slows the wind and reshapes it, diverting it away from high-altitude regions. Finally, we also find that significant circulations/vortices develop over the oceans (see the Indian, Pacific,

and Atlantic Oceans) but these circulations are not symmetric and do not appear to form a standing wave as is typically found on tidally locked exoplanets (Showman & Polvani 2011), suggesting that their driving is more localized than the global driving found with a slab ocean (Braam et al. 2023).

To investigate if this lack of a standing-wave pattern is a robust feature of our model atmospheres or is instead linked to the influence of land/orography on the winds, we next explore the Helmholtz-wind decomposition of the vertically averaged, over all pressure levels, horizontal wind. Starting with the divergent wind (Figures 6(A) and (B)), as previously alluded to, we see evidence for the global overturning circulation with a strong wind diverging from the substellar point and converging on the nightside where it travels downwards. This wind profile is nearly identical in both the SSPO and SSPL models, and shows little to no asymmetry between the Northern and Southern Hemispheres, suggesting that, away from the surface, land/orography has little effect on the divergent component of the wind, and instead it is the strong dayside irradiation which drives the divergent dynamics.

Moving onto the rotational component of the wind, we generally find that the profile is dominated by zonal-mean flows, such as the jets discussed in Section 3.2. As such, in order to visualize the driving forces behind these zonal jets as well as the effects of land/orography on the rotational winds, we further decompose the rotational wind into its zonal-mean and eddy components, plotting the latter component on the bottom row of Figure 6.

Here we can see evidence of two distinct driving forces at play. The first is a standing-wave structure with two circulation cells in each hemisphere, although the exact strength of each cell as well as its extent is location and time dependent. For example, in the SSPO model we find two near-identical circulation cells in the Northern Hemisphere, while in the Southern Hemisphere we find a longitudinally broad anticlockwise circulation cell on the dayside paired with a smaller and weaker clockwise circulation cell on the nightside. A similar, but distinct, story holds true in the SSPL model. Note that the exact structure of the eddy wind is also highly dependent upon the pressure level considered,[4] leading to the asymmetric and pressure-dependent zonal-jet structure discussed in Section 3.2.

Together these changes suggest that the eddy component of the wind, and hence the rotationally driven dynamics (such as the jets discussed in Section 3.2), are much more sensitive to the effects of land and orography. Hence the deviation from the symmetric standing-wave structure predicted by, for example, Williams (1988a) and Showman & Polvani (2011), and found by Carone et al. (2014), Haqq-Misra et al. (2018), and Braam et al. (2023). Examples of these orography induced changes include the slower circulation cell southeast of the substellar point in our SSPO model, a location which approximately corresponds to the location of Australia and the reduced circulation strength north of the substellar point in our SSPL model, a region which approximately corresponds with Europe. In general, these orography induced changes to the Rossby gyres and circulations are in good agreement with those found by Del Genio et al. (2019) for Proxima Centauri b.

[4] This can be seen in the online versions of these figures, which show the divergent and eddy wind components at each pressure level.

3.4. Orography and Horizontal Winds

To better visualize the link between orography and deviations from a symmetric circulation we finish our analysis of the dynamics by exploring the scaler divergence ($\nabla \cdot \boldsymbol{u}$) of the vertically averaged (over all $P > 10^{-1}$ bar) near-surface wind, as shown in Figure 7.

In general, the divergence of the surface wind traces a combination of the orography and the upwelling at the substellar point, with the latter seen as a negative divergence at the center of both panels of Figure 7. Both divergence profiles reveal the high-altitude landmasses discussed in Section 3.3, including winds diverging from the American Cordillera, chaotic mixing over the Tibetan Plateau and mountain ranges on Antarctica, and a previously unmentioned high-latitude mountainous region, Greenland, where we find a strong east–west divergence in the surface wind. Interestingly, the regions which show the largest divergence in the surface wind are also the regions that Bhongade et al. (2024) and Cooke et al. (2024) found that ozone accumulates in, suggesting an orographical explanation for their results.

The strong influence that orography has on the near-surface winds, and in particular its ability to break the symmetry between winds in the Northern and Southern Hemispheres of our otherwise near-symmetric models, suggest that future models of planetary atmospheres need to go beyond just considering the landmass distribution. Instead, as we discuss in Section 4, models also need to consider both the landmass distribution and the orography of the land. Further the possibility that landmasses are breaking the symmetry in atmospheric circulations must be considered when trying to understand unusual observations, such as the potential for asymmetric or concentrated ozone distributions (Braam et al. 2023; Bhongade et al. 2024; Cooke et al. 2024), or the enhancement of disequilibrium chemistry effects due to transport (Chen et al. 2018, 2019). It may also have a role in understanding potential habitability, with studies showing that orography might have shaped the global climate of the early Earth (Liu et al. 2018; Walsh et al. 2019) or driven mass-extinction events (Farnsworth et al. 2023).

3.5. How Atmospheric Circulation Shapes the Surface Distribution of Ozone

We finish our analysis by investigating how the winds and circulations drive the aforementioned asymmetric ozone distribution found in our tidally locked TRAPPIST-1e models. Specifically, as a coda to the work of Bhongade et al. (2024), we explore how cyclonic winds trap ozone at the south pole in both our SSPO and SSPL models.

To aid in this discussion, we transform our grid from the standard latitude–longitude grid used on Earth to the tidally locked coordinate system (Koll & Abbot 2015; Hammond & Lewis 2021), which emphasizes flows between the substellar and antistellar points and around the poles. Under this system, the tidally locked latitude ($\theta_{\rm TL}$) becomes a measure of the angle from the terminator, with the substellar and antistellar points occurring at $\theta_{\rm TL} = 90°$ and $\theta_{\rm TL} = -90°$, respectively. While each tidally locked longitude ($\phi_{\rm TL}$) represents an arc connecting the substellar and antistellar points, passing though the north pole at $\phi_{\rm TL} = 0°$ and $360°$ and the south pole at $\phi_{\rm TL} = 180°$. This can be difficult to visualize at first, hence we provide a diagram in Figure 8 designed to aid the reader in

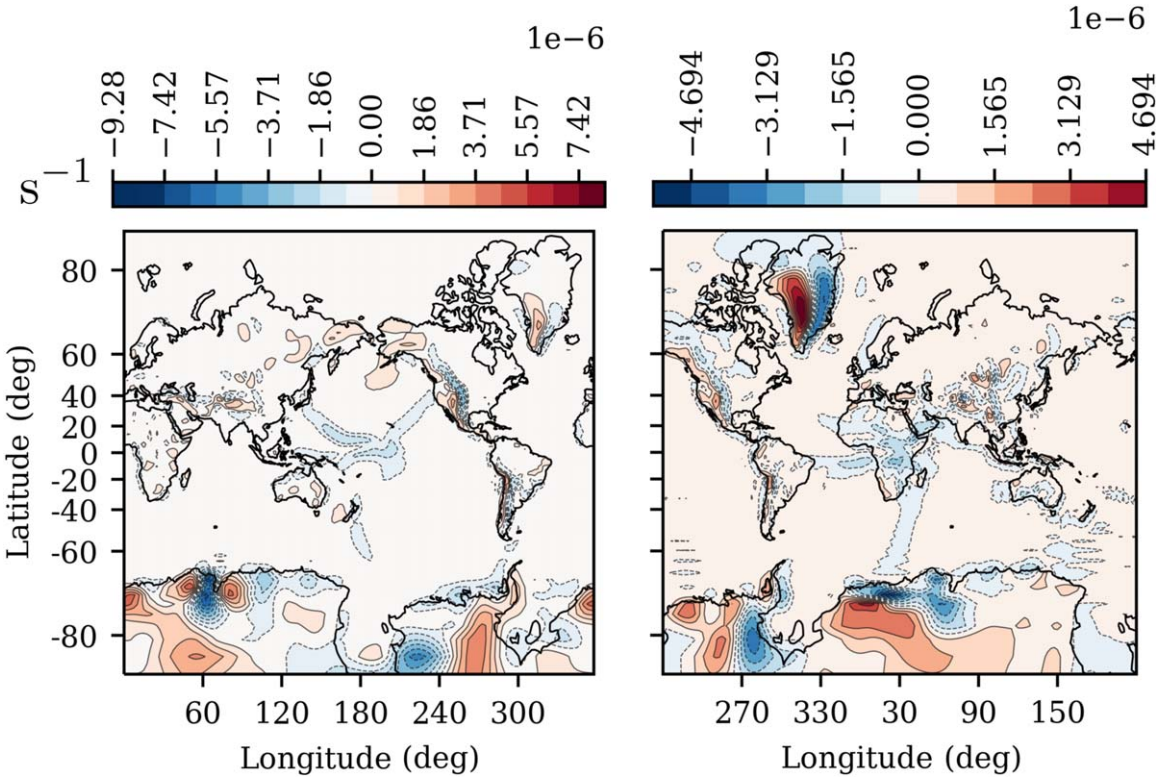

Figure 7. Scalar divergence calculated from the vertically averaged near-surface horizontal winds for both our model with the substellar point placed over the ocean (SSPO; left) and substellar point placed over land/Africa (SSPL; right). The plot uses a Mercator projection to better resolve the divergence field over the Antarctic.

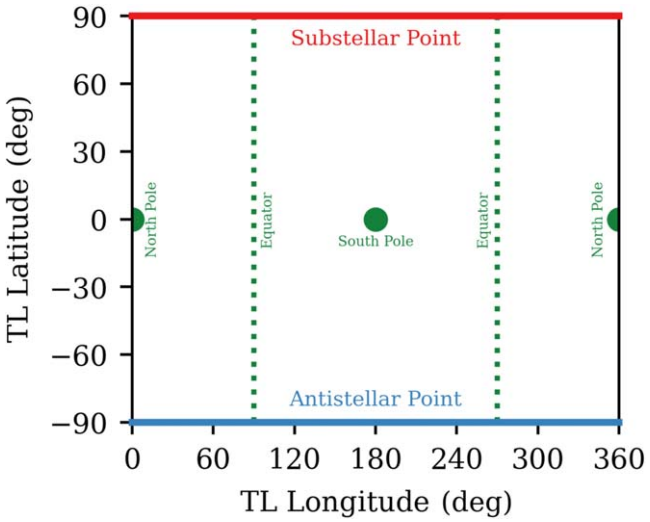

Figure 8. A schematic designed to aid the reader in interpreting horizontal maps plotted in tidally locked coordinates. Here the tidally locked latitude (θ_{TL}) is a measure of the angle from the terminator, with the substellar and antistellar points occurring at $\theta_{TL} = 90°$ and $\theta_{TL} = -90°$, respectively, while each tidally locked longitude (ϕ_{TL}) represents an arc that connects the substellar and antistellar points, passing through the north pole at $\phi_{TL} = 0°$ and the south pole at $\phi_{TL} = 180°$.

interpreting the maps shown in Figure 9. We center our figures on the south pole.

As discussed in Bhongade et al. (2024), ozone forms aloft on the dayside before being transported to the nightside by a combination of the zonal jets and global overturning circulation (Figures 3 and 6). Here the ozone is transported not only down toward the surface but also toward the south pole thanks to the asymmetric meridional circulation (Figure 4), where it accumulates. But why exactly does it become trapped at the south pole and how can such high concentrations accumulate? The answer to the second question is rather simple: the obliquity of TRAPPIST-1e in both of our models is zero, which means that the poles are either dark or weakly illuminated (with any incoming irradiation having to pass through a thick column to reach the near-surface ozone; see Figure 1). As such the polar ozone is relatively stable, and a higher ozone concentration can be maintained (a similar effect occurs in the models of Braam et al. 2023, thanks to their ozone becoming trapped within nightside gyres). Yet this drop in insolation is not enough to explain the high concentrations found in our models (and in the work of Cooke et al. 2024; Bhongade et al. 2024). Much like the nightside gyres of Braam et al. (2023), our results also require that some kind of wind structure confines the ozone to the poles, and in particular to the south pole. We suggest that this takes the form of a polar vortex, with the strong orography of the Antarctic continent driving the enhanced circulation at the south pole.

Evidence for both this wind structure, as well as the role that orography plays in shaping it, can be seen in Figure 9.

Starting slightly further away from the surface (at $P \sim 5 \times 10^{-2}$ bar, ~24 km altitude; Figures 9(A) and (B)), we find vortices at both poles, centered on, and quiescent in, regions of peak ozone concentration. This suggests that the vortices are indeed acting as traps in which ozone accumulates. However differences between the vortices at the north and south poles, and between the SSPO and SSPL models, are apparent. For example, we find that the vortices at the north pole are generally weaker than those at the south pole, reflecting the generally slower zonal-wind speeds found in the Northern Hemisphere (Figure 3). In turn we find that these weaker vortices are less effective at trapping ozone, leading to a

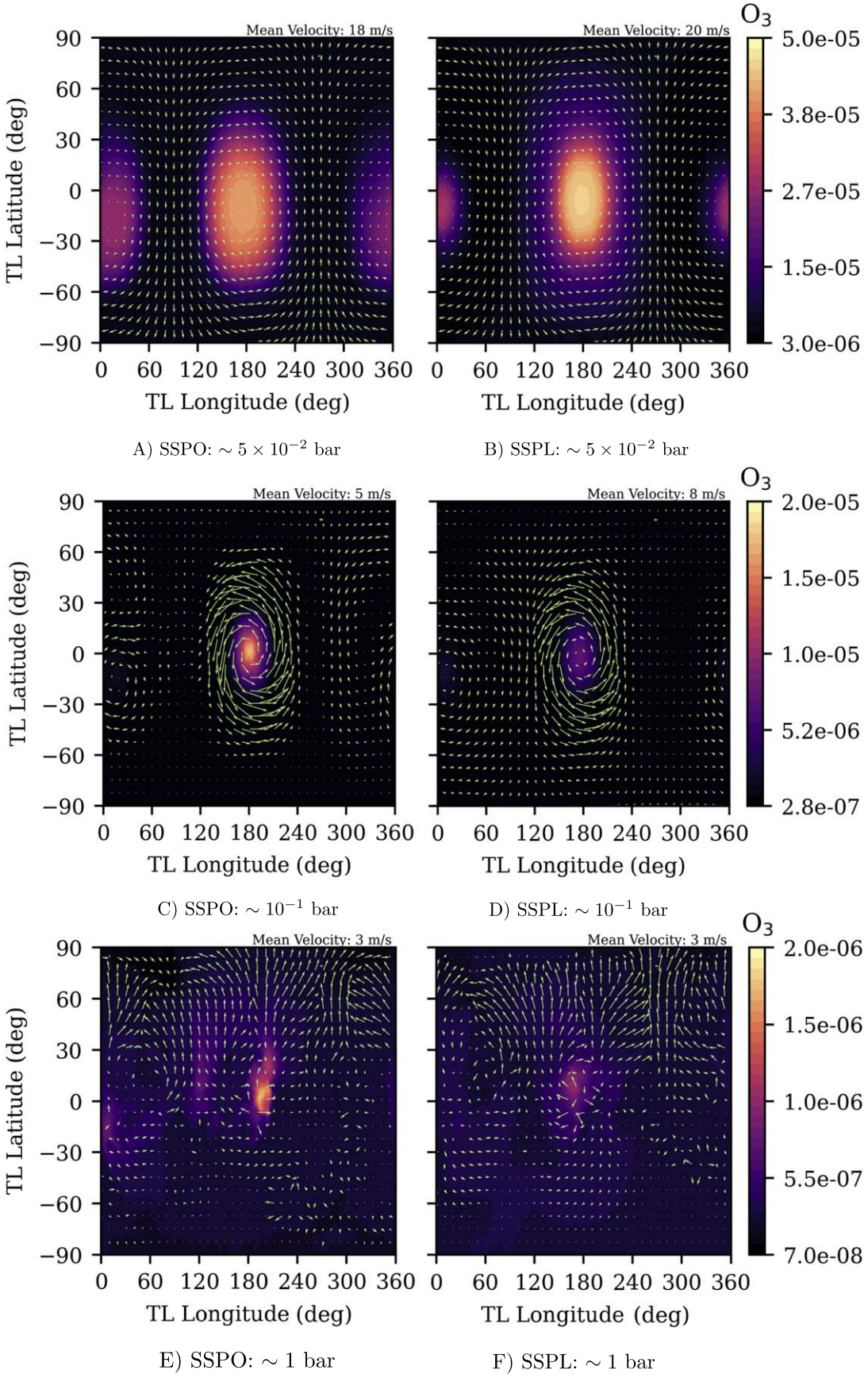

Figure 9. Horizontal slices of the fractional ozone (O_3) abundance at three pressure levels ($\sim 5 \times 10^{-2}$ bar (top), $\sim 10^{-1}$ bar (middle), and ~ 1 bar (bottom)), for both our model with the substellar point placed over the ocean (SSPO; right) and the substellar point placed over land/Africa (SSPL; right). Note that we have transformed the slices to tidally locked coordinates in order to emphasize the buildup of ozone over the poles and the wind/vortices (shown using green quivers), which shape and constrain said buildup.

significant asymmetry between the ozone distribution at the north and south poles, with a much higher ozone concentration found at the south pole. We also find differences between the ozone distribution in our SSPO and SSPL models, although these differences are significantly smaller than that found between the northern and southern poles in both models. For example, while the peak ozone concentration at the south pole is slightly lower in our SSPO than SSPL model, the total ozone concentration at this pressure level is ∼15% higher. This is because of differences in the distribution driven by differences in the relative configuration of the Antarctic landmass in our models. In our SSPO model more of the Antarctic landmass is on the nightside than the dayside, whereas the reverse is true in our SSPL model. In turn, the ozone at the south pole is generally closer to the antistellar point in our SSPO model, further insulating the ozone from any destructive ozone. Note that the differences between the ozone distribution in the SSPO and SSPL models is generally smaller at the north pole than the south pole, reflecting how the north pole is dominated by sea ice in both models.

The asymmetry between the ozone distribution only grows as we move toward the surface ($P \sim 1 \times 10^{-1}$ bar, ∼13.5 km altitude; Figures 9(C) and (D)) and the polar vortex at the north pole starts to weaken and break up. The vortex at the south pole also evolves, with the wind becoming further confined to high latitudes, shrinking the ozone peak and further concentrating ozone at the pole. Differences in the vortex at the south pole, and in the meridional transport more generally (see Section 3.2), then drive differences in the total ozone concentration at 0.1 bar. Not only is the ozone in our SSPO model more concentrated at the pole than in our SSPL model, with a 2× increase in peak ozone abundance, but the total ozone at this pressure level is ∼22% higher in our SSPO model. As for why these differences in polar circulations occur, the most likely cause is a combination of the Coriolis effect and Antarctic katabatic winds: in general Coriolis forces will act to suppress off-equator flows, with the strength of this suppression growing as we move to higher latitudes; however, at the south pole, where the polar plateau induces strong winds from high to low altitudes, we instead find that the Coriolis force acts to reshape the circulation, leading to the observed polar vortex and north–south asymmetry.

Finally, near the surface ($P = 1$ bar, <1 km altitude, Figures 9(E) and (F)), we start to see evidence for the transport of ozone away from the south pole and back toward the equator. In our SSPO model this takes the form of a northeasterly wind transporting ozone from the south pole on the nightside toward the equator on the dayside, while in our SSPL model the wind is more uniformly divergent, leading to the somewhat even transport toward the equator seen in Figure 9(F). Both patterns of ozone transport are compatible with the equatorward surface transport found in the zonal-mean meridional circulation (Figures 4(A) and (B)), emphasizing the need for a multidimensional analysis of the dynamics. Note that the differences in ozone abundance between out SSPO and SSPL models is still present near the surface, with the peak ozone abundance in our SSPO model being ∼50% higher than our SSPL model. However this difference is reduced to ∼2% in favor of our SSPO model when we integrate over the pressure level.

Overall we find that slight differences in the location of the Antarctic landmass, and its associated orography, between our SSPO and SSPL models drive differences in the polar vortex at the south pole. When combined with the differences in atmospheric oxygen content driven the enhanced ocean evaporation in our SSPO model, this can help to explain the highly asymmetric and ozone-rich distributions found in both our models and the models of Cooke et al. (2024).

4. Concluding Remarks

In this work we have used the Earth system model WACCM6/CESM2 to simulate the atmospheric dynamics of the tidally locked, and potentially habitable, terrestrial exoplanet TRAPPIST-1e assuming two different, Earth-like, land–ocean distributions: one in which the substellar point is fixed over the Pacific Ocean (SSPO) and one in which it is fixed over land, specifically central Africa (SSPL). The aim was to investigate how the presence of an Earth-like landmass distribution, with its associated orography, affects the atmospheric dynamics and chemistry. For example, could the inclusion of Earth-like orography explain why both Cooke et al. (2024) and Bhongade et al. (2024) found an asymmetric accumulation of ozone over the south pole whereas Braam et al. (2023, who considered a model with a slab ocean), found a equatorially symmetric ozone distribution with ozone accumulating in off-equator vortices on the nightside. Here we consider models with two different substellar point locations in order to investigate not only the effect of orography on the atmospheric dynamics, but also to distinguish between differences in the atmospheric dynamics associated with the presence of a landmass at the substellar point or due to differences in the land fraction between the Northern and Southern Hemispheres (for Earth-like topography, 68% of the landmass can be found in the Northern Hemisphere). Note that a similar set of landmass distributions for an Earth-like Proxima Centauri b was considered by Del Genio et al. (2019) who found dynamics that were broadly similar to our own, but did not consider a coupled chemistry model, and hence did not identify, for example, the effects of landmass distribution on ozone.

We started our analysis by exploring differences in the zonal-mean atmospheric composition of our two models. We found that the composition of the two models is near indistinguishable, with the differences being primarily associated with the liquid-ocean fraction of the model. These differences occur because, while TRAPPIST-1e is in the habitable zone of its host star, its insolation is about two-thirds of the Earth's, leading to much of its surface being frozen. As such, the only liquid ocean is found near the substellar point and since this region is dominated by a landmass in one of our models (although even here we find liquid oceans near the coast on the dayside), we find significantly stronger ocean evaporation in our SSPO model than our SSPL model. This water acts as a source of atmospheric oxygen, increasing the relative abundance of oxygen-carrying molecules (such as O_3, HO_2, NO_2, etc.), particularly at low pressures where water photodissociates. Note that, the above only holds true because of the Earth-like atmospheric composition of our models. If we were to consider different atmospheric compositions, particularly compositions with increased greenhouse gases, it is possible that both models would be warm enough to maintain significant liquid oceans away from the substellar point (Wolf 2017). However the tidally locked nature of the

insolation means that differences in ocean-surface evaporation rates are likely to persist due to differences in ocean insolation.

We also find that the zonal-wind and meridional circulation profiles are broadly similar between our SSPO and SSPL models. Analysis of the zonal-mean zonal wind reveals that differences between the winds/jets in the Northern and Southern Hemisphere are generally larger than the differences between our SSPO and SSPL models, with the asymmetry peaking in the off-equator jets found near the surface (∼0.5 bar). A similar story also holds true for the zonal-mean meridional circulation. In both our SSPO and SSPL models we find a meridional circulation profile which is dominated by a single cell in each hemisphere, a circulation cell which is reminiscent of the Hadley cells but which extends from the equator to the pole. These circulation cells combine to drive a net upflow slightly north of the equator, similar to the seasonal shift in the Hadley-cell convergence zone on Earth. The presence of a single, rotationally influenced, meridional circulation cell (Hadley cell) per hemisphere is similar to the results reported by, for example, Williams (1988a, 1988b), Navarra & Boccaletti (2002), Carone et al. (2014, 2015), Haqq-Misra et al. (2018), Guendelman & Kaspi (2018), among others. While the circulation structure becomes more complicated when we confine our zonal averages to near the substellar and antistellar points, we still find that the differences between the SSPO and SSPL circulations are small. Furthermore, near the surface, these differences appear to be highly correlated with the landmass distribution. For example, at the substellar point, we find two circulation cells in each hemisphere, with the location of the switch from the Hadley-like cell near the equator and the Ferrel-like cell near the pole occurring at approximately the same latitude that both the SSPO and SSPL models go from being locally land dominated to ocean dominated. Note however that, as we discuss above, the ocean is frozen away from the substellar point. And since it is likely that the interactions between the near-surface wind and sea ice will differ from the interaction with a dynamic liquid ocean, it is possible that a different circulation pattern will be found for a hotter planet. This is something we intend to investigate as part of a future study.

The above differences in the winds and circulations between the Northern and Southern Hemispheres suggested that orography might be playing a significant role in shaping the near-surface winds. We investigated this premise in more detail by exploring the Helmholtz-wind decomposition of both the near-surface and vertically averaged winds. Near the surface, we found that both the divergent and rotational components of the wind revealed significant shaping by landmasses, particularly the presence of orographic features, such as the American Cordillera, the Tibetan Plateau, or the Antarctic mountains. Note that similar continental wind shaping was found by Del Genio et al. (2019) in their Earth-like Proxima Centauri b models. These high-altitude regions also act as sources of wind, for example the katabatic winds which flow from high altitudes to low, winds which can influence the atmospheric composition. The effects of orography of the winds is also present far from the surface, with even the lowest-pressure regions of our atmospheres revealing at least a hint of a north–south asymmetry which is correlated with the landmass distribution and its associated orography. For example, the eddy component of the vertically averaged rotational wind revealed significant differences in the zonal-jet driving standing Rossby and Kelvin wave patterns between both our SSPO and SSPL models, and between the Northern and Southern Hemispheres in both models.

The effects of orography on the near-surface winds and circulations may also help to explain why ozone primarily accumulates at the south pole in both our models and the models of Cooke et al. (2024) and Bhongade et al. (2024): as we approach the surface and the radiative forcing weakens, the Coriolis effect is generally able to suppress high-latitude flows. However at the south pole there is another source of winds, the Antarctic katabatic winds associated with the sharp vertical descent between the Antarctic continent and the surrounding ocean. Rotation reshapes these winds into a vortex, which confines ozone to the south pole (or more specifically over the landmass) almost all the way down to the surface where it then travels equatorward, leading to the lethal surface abundances discussed in Cooke et al. (2024). Further, differences in the orientation of the Antarctic landmass with respect to the substellar point in our SSPL and SSPO models, combined with the relative oxygen content driven by ocean evaporation in our SSPO model, lead to differences in the ozone concentration between $\sim 10^{-2}$ bar and the surface. For example, we found that at $\sim 10^{-1}$ bar the peak ozone concentration in our SSPO model was approximately twice that found in our SSPL model, and even the integrated ozone abundance was ∼22% higher than that found in our SSPL model.

While the above results are interesting, it is important to remember that WACCM6/CESM2 as a model is highly tuned to the Earth's atmosphere. Therefore, care should be taken as the results presented here, and in other work with WACCM6/CESM2, may not be generally applicable. However that does not mean that such models cannot inform us about how heretofore unconsidered planetary features (such as the presence of a dynamic ocean with a complex landmass distribution instead of a highly simplified water world with a shallow, slab ocean and no symmetry breaking orography) might affect planetary atmospheric dynamics, chemistry, potentially habitability, and hence observations.

As such, we suggest that additional development time should be assigned to developing flexible land models, which can be coupled with complex GCMs like WACCM6/CESM2. These flexible land models should allow us to not only explore how changing the landmass fraction between the dayside and nightside and between the Northern and Southern Hemispheres can break the global symmetry in circulations but also to investigate the effects of orography and land-surface composition on the dynamics in more detail. For example, how might the presence of Mars-like mountains (such as Olympus Mons) on a low-mass terrestrial exoplanet affect the dynamics and chemistry, and would such changes be large enough to be observable with future missions? Does the generally low-elevation and ocean-free topography of Venus shape the atmospheric dynamics in a way that is distinct from the Earth? Could cratering and the formation of massive canyons also have a noticeable effect on the dynamics? Or could the presence of a supercontinent, such as that found in both Earth's past and potentially in Earth's future (Davies et al. 2018), drive terrestrial atmospheres away from or toward habitability (Way et al. 2021)? In essence, both other planets in our solar system and our own Earth reveal diverse surfaces and dynamics, and there is no reason to not to expect that this will hold true for extrasolar planets.

Therefore it is safe to say that, as shown by our models, understanding how such landmasses and orography influence the global atmospheric dynamics and hence chemistry may be key to interpreting future observations. This includes assessing if a planet is truly habitable, or if, for example, instead some quirk of the dynamics means that significant, observable ozone (a potential biosignature) can accumulate even when the oxygen content is significantly reduced (Cooke et al. 2023).

Acknowledgments

F.S.-M. and C.W. would like to thank UK Research and Innovation for support under grant No. MR/T040726/1. Additionally, C.W. would like to thank the University of Leeds and the Science and Technology Facilities Council for financial support (ST/X001016/1). This work was undertaken on ARC4, part of the High Performance Computing facilities at the University of Leeds, UK.

ORCID iDs

F. Sainsbury-Martinez https://orcid.org/0000-0003-0304-7931
C. Walsh https://orcid.org/0000-0001-6078-786X
G. J. Cooke https://orcid.org/0000-0001-6067-0979
D. R. Marsh https://orcid.org/0000-0001-6699-494X

References

Agol, E., Dorn, C., Grimm, S. L., et al. 2021, PSJ, 2, 1
Barnes, R. 2017, CeMDA, 129, 509
Baron, E., & Hauschildt, P. H. 2007, A&A, 468, 255
Bhongade, A., Marsh, D. R., Sainsbury-Martinez, F., & Cooke, G. 2024, ApJ, submitted (arXiv:2407.02444)
Braam, M., Palmer, P. I., Decin, L., Cohen, M., & Mayne, N. J. 2023, MNRAS, 526, 263
Broccoli, A. J., & Manabe, S. 1992, JCli, 5, 1181
Carone, L., Keppens, R., & Decin, L. 2014, MNRAS, 445, 930
Carone, L., Keppens, R., & Decin, L. 2015, MNRAS, 453, 2412
Chang, E. K. M., Lee, S., & Swanson, K. L. 2002, JCli, 15, 2163
Chen, H., Wolf, E. T., Kopparapu, R., Domagal-Goldman, S., & Horton, D. E. 2018, ApJL, 868, L6
Chen, H., Wolf, E. T., Zhan, Z., & Horton, D. E. 2019, ApJ, 886, 16
Cheng, W., Macmartin, D., Kravitz, B., et al. 2022, npCAS, 5, 32
Cooke, G. J., Marsh, D. R., Walsh, C., Rugheimer, S., & Villanueva, G. L. 2022, MNRAS, 518, 206
Cooke, G. J., Marsh, D. R., Walsh, C., & Sainsbury-Martinez, F. 2024, PSJ, 5, 168
Cooke, G. J., Marsh, D. R., Walsh, C., & Youngblood, A. 2023, ApJ, 959, 45
Davies, H. S., Green, J. A. M., & Duarte, J. C. 2018, GPC, 169, 133
del Genio, A. D., & Suozzo, R. J. 1987, JAt, 44, 973
Del Genio, A. D., Way, M. J., Amundsen, D. S., et al. 2019, AsBio, 19, 99
Delrez, L., Gillon, M., Triaud, A. H. M. J., et al. 2018, MNRAS, 475, 3577
Dole, S. H. 1964, Habitable Planets for Man (New York: Blaisdell)
Dutton, J. 1986, The Ceaseless Wind: An Introduction to the Theory of Atmospheric Motion (Mineola, New York: Dover)
Emmons, L. K., Schwantes, R. H., Orlando, J. J., et al. 2020, JAMES, 12, e2019MS001882
Farnsworth, A., Lo, Y. T. E., Valdes, P. J., et al. 2023, NatGe, 16, 901
Fauchez, T. J., Villanueva, G. L., Sergeev, D. E., et al. 2022, PSJ, 3, 213
Gettelman, A., Mills, M. J., Kinnison, D. E., et al. 2019, JGRD, 124, 12380
Gillon, M., Jehin, E., Fumel, A., Magain, P., & Queloz, D. 2013, in EPJ Web of Conf. 47, Hot Planets and Cool Stars, ed. R. Saglia (Garching: EDP Sciences), 03001
Gillon, M., Jehin, E., Lederer, S. M., et al. 2016, Natur, 533, 221
Grimm, S. L., Demory, B.-O., Gillon, M., et al. 2018, A&A, 613, A68
Guendelman, I., & Kaspi, Y. 2018, GeoRL, 45, 213
Hammond, M., & Lewis, N. T. 2021, PNAS, 118, e2022705118
Haqq-Misra, J., Wolf, E. T., Joshi, M., Zhang, X., & Kopparapu, R. K. 2018, ApJ, 852, 67
Hauschildt, P. 1993, JQSRT, 50, 301
Hauschildt, P. H., & Baron, E. 2006, A&A, 451, 273
Hoskins, B. J., & Valdes, P. J. 1990, JAtS, 47, 1854
Hu, Y., & Yang, J. 2014, PNAS, 111, 629
Kammerer, J., Quanz, S. P., Dannert, F. & LIFE Collaboration 2022, A&A, 668, A52
Knutson, H. A., Charbonneau, D., Allen, L. E., et al. 2007, Natur, 447, 183
Koll, D. D. B., & Abbot, D. S. 2015, ApJ, 802, 21
Kopparapu, R. K., Ramirez, R., Kasting, J. F., et al. 2013, ApJ, 765, 131
Krissansen-Totton, J., Galloway, M. L., Wogan, N., Dhaliwal, J. K., & Fortney, J. J. 2021, ApJ, 913, 107
Laurila, T. K., Gregow, H., Cornér, J., & Sinclair, V. A. 2021, WCD, 2, 1111
Liu, B., Marsh, D. R., Walsh, C., & Cooke, G. 2023, MNRAS, 524, 1491
Liu, Y., Peltier, W. R., Yang, J., & Hu, Y. 2018, JCli, 31, 8463
Lustig-Yaeger, J., Meadows, V. S., & Lincowski, A. P. 2019, AJ, 158, 27
Macdonald, E., Menou, K., Lee, C., & Paradise, A. 2024, MNRAS, 529, 550
Macdonald, E., Paradise, A., Menou, K., & Lee, C. 2022, MNRAS, 513, 2761
National Academies of SciencesEngineering, and Medicine 2023, Pathways to Discovery in Astronomy and Astrophysics for the 2020s (Washington, D. C.: The National Academies Press)
Navarra, A., & Boccaletti, G. 2002, ClDy, 19, 467
Peacock, S., Barman, T., Shkolnik, E. L., Hauschildt, P. H., & Baron, E. 2019, ApJ, 871, 235
Pepin, N. C., Arnone, E., Gobiet, A., et al. 2022, RvGeo, 60, e2020RG000730
Pierrehumbert, R. T. 2011, ApJL, 726, L8
Salazar, A. M., Olson, S. L., Komacek, T. D., Stephens, H., & Abbot, D. S. 2020, ApJL, 896, L16
Sandu, I., van Niekerk, A., Shepherd, T. G., et al. 2019, npCAS, 2, 10
Sergeev, D. E., Fauchez, T. J., Turbet, M., et al. 2022, PSJ, 3, 212
Showman, A. P., & Guillot, T. 2002, A&A, 385, 166
Showman, A. P., & Polvani, L. M. 2011, ApJ, 738, 71
Turbet, M., Fauchez, T. J., Sergeev, D. E., et al. 2022, PSJ, 3, 211
Waliser, D., & Jiang, X. 2015, in Encyclopedia of Atmospheric Sciences, ed. G. R. North, J. Pyle, & F. Zhang (2nd ed.; Oxford: Academic Press), 121
Walsh, A., Ball, T., & Schultz, D. M. 2019, NatSR, 9, 2349
Way, M. J., Davies, H. S., Duarte, J. C., & Green, J. A. M. 2021, GGG, 22, e09983
Williams, G. P. 1988a, ClDy, 2, 205
Williams, G. P. 1988b, ClDy, 3, 45
Wolf, E. T. 2017, ApJL, 839, L1
Xian, T., Xia, J., Wei, W., et al. 2021, Atmos, 12, 1699
Zellem, R. T., Lewis, N. K., Knutson, H. A., et al. 2014, ApJ, 790, 53